energies

MDPI

Article

Research on Off-Design Characteristics and Control of an Innovative S-CO_2 Power Cycle Driven by the Flue Gas Waste Heat

Shaohua Hu [1], Yaran Liang [1], Ruochen Ding [2], Lingli Xing [3], Wen Su [1,*], Xinxing Lin [2] and Naijun Zhou [1]

[1] School of Energy Science and Engineering, Central South University, Changsha 410083, China; 223911012@csu.edu.cn (S.H.); 213911016@csu.edu.cn (Y.L.); njzhou@csu.edu.cn (N.Z.)
[2] China Three Gorges Corporation Science and Technology Research Institute, Beijing 100038, China; ding_ruochen@ctg.com.cn (R.D.); lin_xinxing@ctg.com.cn (X.L.)
[3] Hunan Province College Key Laboratory of Molecular Design and Green Chemistry, Hunan University of Science and Technology, Xiangtan 411201, China; xinglingli@hnust.edu.cn
* Correspondence: suwenzn@csu.edu.cn

Abstract: Recently, supercritical CO_2 (S-CO_2) has been extensively applied for the recovery of waste heat from flue gas. Although various cycle configurations have been proposed, existing studies predominantly focus on the steady analysis and optimization of different S-CO_2 structures under design conditions, and there is a noticeable deficiency in off-design research, especially for the innovative S-CO_2 cycles. Thus, in this work aimed at the proposed novel S-CO_2 power cycle, off-design characteristics and corresponding control strategies are investigated for the waste heat recovery. Based on the design parameters of the S-CO_2 cycle, structural dimensions of printed circuit heat exchangers (PCHEs) and shell-and-tube heat exchangers are determined, and design values of turbines and compressors are specified. On this basis, off-design models for these key components are formulated. By manipulating variables such as cooling water inlet temperature, cooling water mass flow rate, flue gas inlet temperature and flue gas mass flow rate, cycle performances of the system are analyzed under off-design conditions. The simulation results show that when the inlet temperature and the mass flow rate of cooling water vary separately, the thermal efficiency both can reach the maximum value of 28.43% at the design point. For the changes in heat source parameters, the optimum point is slightly deviated from the design condition. Amidst the fluctuations in flue gas inlet temperature, the thermal efficiency optimizes to a peak of 28.56% at 530 °C. In the case of variation in the flue gas mass flow rate, the highest thermal efficiency 28.75% can be obtained. Furthermore, to maintain the efficient and stable operation of the S-CO_2 power cycle, the corresponding control strategy of the cooling water mass flow rate is proposed for the cooling water inlet temperature variation. Generally, when the inlet temperature of cooling water increases from 23 °C to 27 °C, the cooling water mass flow should increase from 82.3% to 132.7% of the design value to keep the system running as much as possible at design conditions.

Keywords: off-design condition; flue gas waste heat; S-CO_2 power cycle; control strategy

check for updates

Citation: Hu, S.; Liang, Y.; Ding, R.; Xing, L.; Su, W.; Lin, X.; Zhou, N. Research on Off-Design Characteristics and Control of an Innovative S-CO_2 Power Cycle Driven by the Flue Gas Waste Heat. *Energies* **2024**, *17*, 1871. https://doi.org/10.3390/en17081871

Received: 29 February 2024
Revised: 2 April 2024
Accepted: 9 April 2024
Published: 14 April 2024

1. Introduction

1.1. Background

Currently, fossil fuel energy is still the main source of energy with the increase in primary energy consumption. However, the burning of coal, oil and other fossil fuels generates a high amount of environmentally unfriendly gases, among which carbon dioxide causes a serious greenhouse effect [1,2]. To alleviate the dilemma of energy scarcity while reducing the environmental impact of fossil fuels, it is imperative to enhance energy efficiency. The waste heat from industrial waste gas has great recovery potential, and scholars have extensively conducted research on the comprehensive recovery and optimal utilization of industrial waste heat without interfering with the original industrial manufacturing process [3,4]. The organic Rankine cycle (ORC) holds a pivotal position in the realm of low temperature thermal power generation due to the low critical parameters of the organic working fluid [5,6]. Although ORC is a mature technology that offers the advantages of low maintenance costs, high operating pressure and autonomous operation, it still suffers from disadvantages such as a low boiling point of organic working fluid, low waste heat recovery efficiency, environmental pollution and safety issues [7,8]. In the case of high-temperature waste heat utilization, the technically mature steam Rankine cycle is usually used. However, the steam Rankine cycle has high heat loss, a large component volume and high system cost [9]. In recent years, in view of the shortcomings of the existing steam Rankine cycle and the low critical parameters of CO_2 (Tc = 30.98 °C, Pc = 7.38 MPa), scholars have proposed the application of the supercritical CO_2 (S-CO_2) Brayton power cycle to recover the waste heat of high temperature flue gas [10,11]. In contrast with the steam Rankine cycle, the S-CO_2 cycle has the advantages of a compact system structure, a low cost and high cycle efficiency [12].

1.2. Study on S-CO_2 Cycle Layout and Performance

In order to improve thermal efficiency, scholars in various countries have conducted many studies on optimizing the S-CO_2 cycle. One approach is to combine thermodynamic processes such as multi-stage compression, segmented expansion and reheating on the basis of a simple S-CO_2 cycle [13,14]. Several typical layouts of S-CO_2 cycles have been formed, including the simple recuperative cycle (SRC), the recompression cycle (RC), the precompression cycle (PC), the partial cooling cycle (PCC), the intermediate cooling cycle (ICC), and their layouts with reheating. Liao et al. analyzed five types of cycles and compared the cycle efficiencies of the five cycle systems under the same operating parameters, which showed that both the recompression cycle and the partial cooling cycle exhibit superior efficiency, while no significant advantage in efficiency is observed for the partial cooling cycle under low pressure ratios [15]. Fang et al. introduced a waste heat recovery system predicated on the split expansion cycle. Compared to the conventional recompression cycle, the fuel utilization rate of a 1 MW natural gas engine increases by 14.9%, while achieving the net power and heat recovery rates of 174.2 kW and 58%, respectively [16]. Another enhancement approach involves designing a combined cycle layout with the S-CO_2 cycle serving as the top cycle [13]. Given that the primary function of the bottom cycle is to capture low-grade waste heat from the top cycle, the transcritical CO_2 cycle (T-CO_2), ORC, and refrigeration cycle are all integrated with the S-CO_2 cycle, forming well-combined cycles. Fu used the S-CO_2 Brayton cycle as the top cycle and combined it with an ORC system or a T-CO_2 cycle system to establish a combined cycle with different layouts. The performance of the combined cycle exhibited notable enhancements compared to the stand-alone S-CO_2 Brayton cycle. Moreover, in the recompression S-CO_2/ORC combined cycle, system efficiency reached its peak when employing isopentane as the working fluid in the ORC [17]. The above research results show that the improvement of thermal efficiency is closely related to the S-CO_2 cycle structure, and the different configuration of the cycle system has a crucial impact on the performance of the cycle.

1.3. Study on Off-Design Performance of S-CO_2 Cycle

The above studies, all analyzed with the key system parameters unchanged, evaluated the steady-state performance of different S-CO_2 systems. In practical applications, the performances of systems are likely to vary due to the fluctuations in cold and heat source conditions influenced by environmental changes. To advance the practical engineering application of the S-CO_2 power cycle, it is imperative to analyze and study the performance characteristics of the cycle under off-design conditions, so as to solve the problems that may occur in the actual operation of the system. Andrew et al. studied the off-design operation of the S-CO_2 cycle by utilizing head and efficiency curves proposed by Dyreby. They modified the dimensionless compression ratio and isentropic efficiency of the compressor based on these curves to characterize the performance characteristics of the compressor under off-design operating conditions [18]. Duniam et al. conducted a study examining the influence of ambient temperature at design values on the operational performance of the S-CO_2 recompression Brayton cycle under off-design conditions. The results showed that the lower the design value, the higher the peak efficiency. However, the declines in efficiency are greater with the increase in ambient temperature, and the benefit of low ambient temperature is limited when the design values are higher [19]. In conclusion, these existing studies focus more on the off-design performance analysis of typical S-CO_2 cycles and system components, and there is still a lack of studies on off-design conditions for novel S-CO_2 cycles.

1.4. Purpose of This Work

The system can run efficiently and stably by adjusting the key parameters when the external conditions change, so it is necessary to study the off-design characteristics of the cycle. Based on an innovative S-CO_2 power cycle driven by flue gas waste heat proposed by our research group [20], off-design characteristics and corresponding control strategies are studied in this paper. Based on the design parameters of the S-CO_2 cycle, along with the determined structural parameters of heat exchangers and performance parameters of the turbomachinery, off-design mathematical models are developed for the system components. Subsequently, according to the simulation results, the performance characteristics of the system are analyzed when the parameters of cold and hot sources change. In addition, since the cooling water inlet temperature is prone to affect the cycle performance, a cooling water mass flow rate control strategy is proposed to ensure the stable and efficient operation of the cycle.

2. System Layout and Design Parameters

Figure 1 illustrates the layout of the S-CO_2 power cycle driven by flue gas waste heat, and the corresponding *T*-*s* diagram is shown in Figure 2. S-CO_2 is divided into two streams at the outlet of the cooler. One stream is compressed in Compressor1 (5–6), and then successively flows into the high-pressure side of the low-temperature recuperator (LTR, 6–7) and the high-temperature recuperator (HTR, 7–8) to be heated. After that, S-CO_2 further absorbs waste heat from the flue gas in Heater1, expanded to carry out work in the high-pressure turbine (HPT, 1–2), and finally cooled by HTR (2–3), LTR (3–4), and the cooler (4–5). Another stream of S-CO_2 is first compressed in Compressor2 (5–9), and then heated by the flue gas in Heater2 (9–10). After being heated, S-CO_2 is expanded into the low-pressure turbine (LPT, 10–3) to carry out work, and finally S-CO_2 is mixed with another stream of fluid at the low-pressure outlet of HTR.

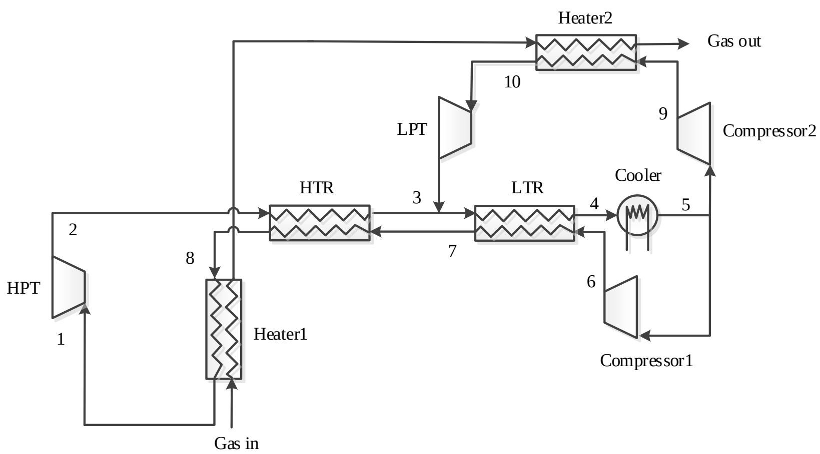

Figure 1. Layout diagram of the system.

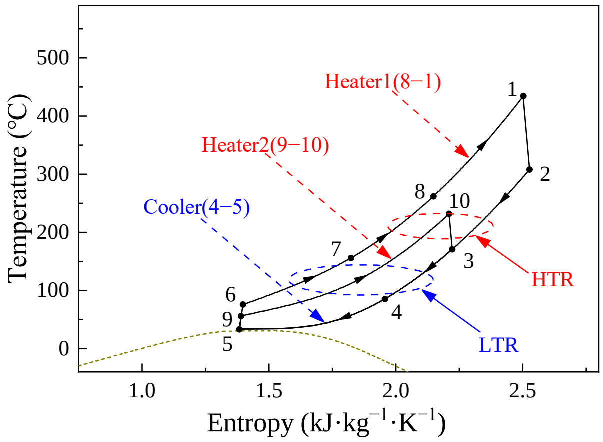

Figure 2. Temperature entropy diagram of the system.

The composition and parameters of the flue gas are obtained from a diesel engine, as shown in Table 1. Besides the components listed in Table 1, the flue gas mixture also contains SO_2, SO_3, NO_X and other components. However, they are not included in the table because of the extremely low content and small impact on the heat transfer characteristics of the flue gas.

Table 1. Main parameters of flue gas [20,21].

Flue Gas Components	Value	Flue Gas Parameters	Value
N_2 (%)	71.6	Flue gas inlet temperature (°C)	520
CO_2 (%)	15.1	Flue gas mass flow (kg/s)	20
O_2 (%)	7.8	Flue gas pressure (MPa)	0.1
H_2O (%)	5.5		

For the cycle, the parameters of design conditions are shown in Table 2. The high pressure, medium pressure and low pressure of the cycle are set to be 25 MPa, 15 MPa and 7.8 MPa, respectively. The compressor inlet temperature represents the minimum cycle temperature, which is set at 33 °C. For the pinch point temperature difference (PPTD), considering the heat exchange efficiency and heat exchanger economy, the PPTD of the heat exchangers are set above 5 °C. Under the design conditions, the parameters of each state point of the cycle are shown in Table 3.

Table 2. System standard design conditions.

Design Parameters	Value
HPT inlet temperature (°C)	434.35
Compressor inlet temperature (°C)	33
HPT inlet pressure (MPa)	25
LPT inlet pressure (MPa)	15
Compressor inlet pressure (MPa)	7.8
PPTD of Heater1 (°C)	20
PPTD of Heater2 (°C)	20
PPTD of HTR (°C)	≥5
PPTD of LTR (°C)	≥5
Isentropic efficiency of Compressor [20]	0.85
Isentropic efficiency of Turbine [20]	0.9
Energy efficiency coefficient of heat exchanger [20]	0.9

Table 3. Parameters of each state point of the cycle.

State Point	*m* (kg/s)	*P* (MPa)	*T* (°C)	*s* (kJ/(kg·K))	*h* (kJ/kg)
1	24.44	25	434.35	2.5	887.36
2	24.44	7.8	307.9	2.53	762.17
3	37.94	7.8	170.52	2.22	606.76
4	37.94	7.8	85.16	1.96	501.11
5	37.94	7.8	33	1.38	318.06
6	24.44	25	75.32	1.4	349.02
7	24.44	25	155.6	1.82	513.01
8	24.44	25	261.73	2.15	668.43
9	13.5	15	55.66	1.39	331.95
10	13.5	15	231.66	2.21	654.43
Flue gas inlet	20	0.1	520	7.2	959.9
Flue gas outlet of Heater1	20	0.1	281.73	6.8	692.32
Flue gas outlet	20	0.1	75.69	6.31	474.63
cooling water inlet	110.79	0.1	25	0.37	104.92
cooling water outlet	110.79	0.1	40	0.57	167.62

For the performances of the S-CO_2 Brayton cycle, the evaluation indexes include the thermal efficiency (η_{th}) and net output work (W_{net}) of the cycle. In order to obtain these data, the expansion work, compression work and total heat absorption of the cycle should be calculated.

The W_{net} is the difference between the work of expansion and the work of compression, which can be expressed by

$$W_{net} = W_{HPT} + W_{LPT} - W_{Compressor1} - W_{Compressor2} \tag{1}$$

The η_{th} is the ratio of W_{net} to the total heat absorbed by the flue gas heat source, which is calculated as follows:

$$\eta_{th} = \frac{W_{net}}{Q_{Heater1} + Q_{Heater2}} \tag{2}$$

3. Structural Design and Off-Design Models of Heat Exchangers

The heat exchangers in the system include a cooler, two heaters and two recuperators. The fluids used in the heat exchangers include CO_2, flue gas and water. To simplify heat transfer calculations, thermodynamic modeling makes the following assumptions:

- The pressure drop of the heat exchangers caused by inlet losses, outlet losses and acceleration effects is neglected.
- The fluids are fully mixed in the tube and flow one-dimensionally.
- The heat conduction between the fluids and the tube wall along the axial direction is ignored.
- The heat transfer with the external environment is ignored.

Based on the above assumptions and the heat transfer condition of the cycle, printed circuit heat exchangers (PCHEs) and shell-and-tube heat exchangers are used to complete the heat transfer in the system.

3.1. Structural Design of Heat Exchangers

The off-design performances of the system are affected by the capacity constraints of the system components. Therefore, the heat exchangers should first be designed. The structural design parameters of PCHEs and shell-and-tube heat exchangers are obtained by calculating the parameters of each state point under the design conditions, as shown in Tables 4 and 5.

Table 4. Structural design parameters of PCHEs.

Parameters	HTR	LTR	Cooler
Channel width (mm)	1	1	1
Channel depth (mm)	1	1	1
Plate thickness (mm)	1.5	1.5	1.5
Fin width (mm)	0.5	0.5	0.5
Number of channels per layer	300	300	300
Number of plies	300	300	300
Single channel heat transfer area (m^2)	0.025	0.05	0.036

Table 5. Structural design parameters of shell-and-tube heat exchangers.

Parameters	Heater1	Heater2
Number of one-way tubes	484	237
One way tube length (m)	16.64	40.44
Length of tube (m)	5	7
Number of tube sides	4	6
Number of shell sides	2	2
Number of centerline tubes	48	41
Calculated nominal diameter (m)	1.77	1.51
Nominal diameter (m)	1.8	1.6
Inside diameter of tube (m)	0.02	0.02
Outer diameter of tube (m)	0.025	0.025
Tube wall thickness (m)	0.0025	0.0025
Tube pitch (m)	0.032	0.032
Pipe flow area (m^2)	0.0003	0.0003
Baffle thickness (m)	0.012	0.012
Baffle spacing (m)	0.3	0.3
Number of baffles	52	126
Total heat transfer area (m^2)	596.97	706.9
Area margin	17.20%	1.65%
CO_2 tube velocity (m/s)	0.75	0.75
Flue gas center velocity (m/s)	204.26	142.83
Pipe pressure drop (kPa)	7.93	17.41
Pipe volume (m^3)	3.04	3.13
Heat transfer coefficient of CO_2 (W/(m^2·k))	535.34	575.07
Heat transfer coefficient of flue gas (W/(m^2·k))	380.22	324.64

3.2. Off-Design Models of Heat Exchangers

3.2.1. Off-Design Models of PCHEs

Compared with traditional heat exchangers, micro-channel heat exchangers can significantly reduce the volume and greatly enhance the heat transfer efficiency while maintaining the same heat transfer capacity. In this way, they have been widely used in many important fields. Among them, PCHE is widely used in the S-CO_2 energy system due to its advantages of high-temperature and high-pressure resistance, high compactness and high reliability [22]. Therefore, the HTR and LTR of the S-CO_2 cycle adopt counter current S-shaped fin PCHEs. For the cooler, the S-CO_2 fluid is cooled by water cooling. The density of water at normal temperature and pressure is the same order of magnitude as that of S-CO_2, and the treated water has less corrosion on the PCHE micro-channels. Thus, the cooler of the system uses the same PCHE as the recuperators. Taking into account periodic boundary conditions, the PCHE model is simplified to a single channel. It consists of a hot and a cold side channel. Furthermore, the heat transfer parameters of each channel unit in a single layer are considered to be the same [23].

The single channel unit heat transfer rate Q_{ch} is:

$$Q_{ch} = \frac{Q}{a} \tag{3}$$

where Q is the total heat transfer rate, and a is the total number of channel units of cold or hot fluid [24].

As shown in Figure 3, the inlet temperatures of the hot and cold fluids of the PCHE are $T_{\mathrm{h,in}}$ and $T_{\mathrm{c,in}}$, respectively. A single channel unit is divided into n segments along the flow direction, and each segment is regarded as a separate subunit. The heat transfer rate of each subunit $Q_{\mathrm{ch,i}}$ is formulated as:

$$Q_{\mathrm{ch,i}} = \frac{Q_{\mathrm{ch}}}{n} \tag{4}$$

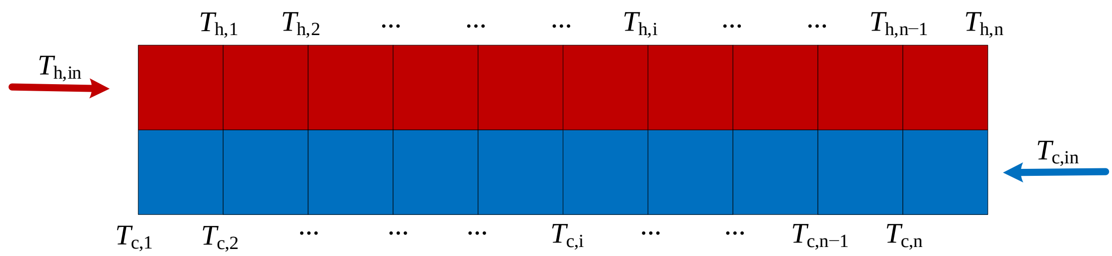

Figure 3. Schematic diagram of counter current PCHE heat transfer channel unit.

Based on the parameters of each heat exchange subunit, the heat exchange area $A_{\mathrm{ch,i}}$ can be calculated as

$$A_{\mathrm{ch,i}} = \frac{Q_{\mathrm{ch,i}}}{k_{\mathrm{i}} \cdot \Delta T_{\mathrm{i}}} \tag{5}$$

where ΔT_{i} represents the arithmetic average temperature difference between the cold and hot streams in section i, and k represents the local heat transfer coefficient, which can be expressed by Equation (6).

$$k = \frac{1}{\frac{1}{h_{\mathrm{h}}} + R_{\mathrm{w}} + \frac{1}{h_{\mathrm{c}}}} \tag{6}$$

where R_{w} denotes the thermal resistance of the channel wall, h_{h} and h_{c} represent the convective heat transfer coefficients of hot and cold fluids, respectively.

The convective heat transfer coefficient h can be expressed in the following way:

$$h = \frac{\lambda \cdot Nu}{d_{\mathrm{hy}}} \tag{7}$$

where λ denotes the thermal conductivity of the fluid and d_{hy} denotes the hydraulic diameter of the channel.

The heat transfer correlations used for the PCHE models in the system are shown in Table 6.

Table 6. Heat transfer correlations of PCHE models.

Category	Heat Transfer Correlations	References
The S-CO_2 side of LTR, HTR, and cooler	$Nu = 0.174Re^{0.593}Pr^{0.43}$	[23,25]
The water side of cooler	$Nu = \frac{\frac{f}{8}(Re-1000)Pr}{1+12.7\sqrt{\frac{f}{8}}\left(Pr^{2/3}-1\right)}$, $2300 \le Re \le 10^6$, $0.6 \le Pr \le 10^5$ $f = (0.79 \times \ln(Re) - 1.64)^{-2}$	[26]

Channel hydraulic diameter d_{hy} can be represented by Equation (8).

$$d_{\mathrm{hy}} = \frac{2 \cdot w_{\mathrm{ch}} \cdot d_{\mathrm{ch}}}{w_{\mathrm{ch}} + d_{\mathrm{ch}}} \tag{8}$$

where w_{ch} is the channel width and d_{ch} is the channel height. Based on these two parameters, the flow area A_{flow} of the channel can be calculated as

$$A_{flow} = w_{ch} \cdot d_{ch} \tag{9}$$

Channel wall thermal resistance R_w can be expressed as

$$R_w = \frac{t_p - d_{ch}}{\lambda_w} \tag{10}$$

where t_p represents the thickness of the heat exchange plate, λ_w represents the thermal conductivity of the wall of the channel.

The total heat transfer area A_{ch} of a single channel is expressed as

$$A_{ch} = \sum_{i=1}^{n} A_{ch,i} \tag{11}$$

The actual heat exchanger area of the PCHE is determined under the design condition. Under off-design conditions, a trial-and-error method is employed to determine the outlet temperatures of the PCHE based on the calculated heat transfer area.

3.2.2. Off-Design Models of Shell-and-Tube Heat Exchangers

For the heaters, the heat source is high-temperature flue gas. The flue gas has a large density gap with S-CO_2, and contains acidic gas, which will corrode the micro-channel of the heat exchanger, so PCHE is not suitable. Therefore, the shell-and-tube heat exchanger with a baffle shell is selected for the heaters in this paper, and its heat exchange tubes are arranged in a positive triangle mode, as shown in Figure 4.

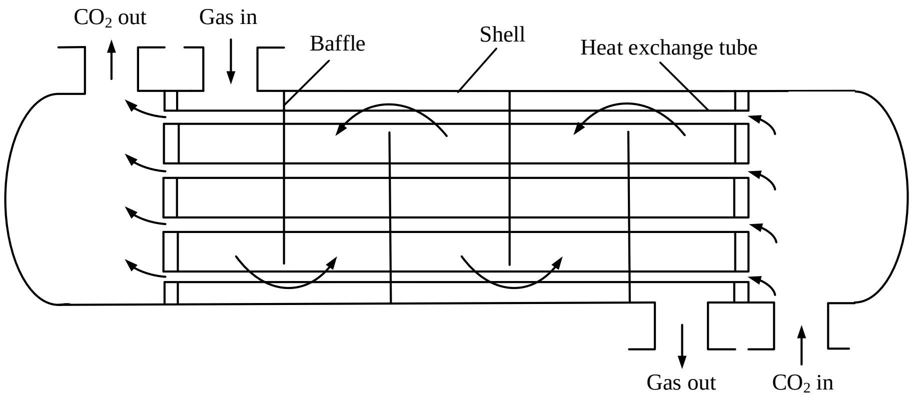

Figure 4. Schematic diagram of shell-and-tube heat exchanger.

The steady-state heat transfer equation of the hot fluid through a fixed wall surface is given by

$$Q = K \cdot A \cdot \Delta T \tag{12}$$

where Q is the heat transfer rate, K is the total heat transfer coefficient, A is the heat transfer area, and ΔT is the average heat transfer temperature difference.

The total heat transfer coefficient K can be calculated from Equation (13) without considering the influence of fouling thermal resistance inside and outside the pipe.

$$K = \frac{1}{\frac{1}{\alpha_o} + \frac{1}{\alpha_i}\left(\frac{A_o}{A_i}\right) + \frac{\delta A_o}{\lambda_w A_m}} \tag{13}$$

where α_i and α_o, respectively, represent the heat transfer coefficient inside and outside the tube, λ_w is the thermal conductivity of the tube wall, δ represents the thickness of the tube wall, A_i, A_o and A_m are, respectively, the heat transfer area inside and outside the heat transfer tube and the average heat transfer area.

For shell-and-tube heat exchangers, the tube heat transfer coefficient is related to the flow state, which is usually expressed by *Re*. The heat transfer correlations are shown in Table 7.

Table 7. Heat transfer correlations of shell-and-tube heat exchanger models.

Category	Heat Transfer Correlations	References
S-CO_2 side	$\alpha = 0.023\frac{\lambda}{d}Re^{0.8}Pr^{\mathrm{n}}, Re > 10^4, 0.7 < Pr < 120, L/d \geq 60$	[27]
	$\alpha = 0.023(1-\frac{6\times10^5}{Re^{1.8}})\frac{\lambda}{d}Re^{0.8}Pr^{n}, 2300 < Re < 10^4$	[28]
	$Nu = 1.86Re^{1/3}Pr^{1/3}\left(\frac{d_i}{L}\right)^{1/3}\left(\frac{\mu_i}{\mu_w}\right)^{0.14}, Re < 2300$	[29]
Flue gas side	$\alpha_o = 0.36\frac{\lambda}{d_e}\left(\frac{d_e u_o \rho}{\mu}\right)^{0.55}Pr^{1/3}\left(\frac{\mu}{\mu_w}\right)^{0.14}, 2000 < Re < 10^6$	[30]

For the n in Table 5, n is set to be 0.4 when the fluid is heated, while n is set to be 0.3 when the fluid is cooled.

d_e denotes the feature size, which can be calculated by the following formula:

$$d_\mathrm{e} = \frac{1.1{P_\mathrm{t}}^2}{d_\mathrm{o}} - d_\mathrm{o} \tag{14}$$

where P_t denotes the center distance of the heat exchange tube and d_o denotes the outer diameter of the heat exchange tube.

The maximum cross-sectional area between tubes A_s can be expressed as

$$A_\mathrm{s} = l_\mathrm{b}D_\mathrm{i}\left(1 - \frac{d_\mathrm{o}}{P_\mathrm{t}}\right) \tag{15}$$

where l_b represents the baffle spacing and D_i represents the inner diameter of the shell of the heat exchanger.

n_c represents the number of tubes across the centerline of the bundle, and for a triangular arrangement, n_c can be expressed as

$$n_\mathrm{c} = 1.1\sqrt{N_\mathrm{t}} \tag{16}$$

where N_t represents the number of heat exchange tubes.

Shell side flow area A_f can be expressed as

$$A_\mathrm{f} = l_\mathrm{b}(D_\mathrm{i} - n_\mathrm{c}d_\mathrm{o}) \tag{17}$$

The heat transfer area of shell-and-tube heat exchanger is calculated differently from the PCHE, but the same trial-and-error method is used for off-design modeling.

4. Off-Design Models of the Power Machinery

In most current simulation studies, the isentropic efficiency of turbomachinery is usually assumed to be constant. It is applicable solely for calculating steady-state design conditions and is not suitable for analyzing off-design conditions. Under off-design conditions, when the external conditions change, the isentropic efficiency of the turbine and compressor in the S-CO_2 cycle changes dramatically with the change in key parameters [31]. Therefore, in order to meet the requirements of off-design conditions, it is necessary to modify the isentropic efficiency of turbomachinery. In this section, the mathematical models of compressor and turbine under off-design conditions are established. The isentropic efficiency varies with the basic operating parameters such as temperature, mass flow rate, pressure and speed [32,33].

4.1. Modeling of Compressor

For compressors, the isentropic efficiency η_C under off-design conditions can be expressed by

$$\frac{\eta_C}{\eta_{C,d}} = \left[1 - c_4 \times \left(1 - \dot{N}\right)^2\right] \left(\frac{\dot{N}}{\dot{m}}\right) (2 - \frac{\dot{N}}{\dot{m}}) \tag{18}$$

where $\eta_{C,d}$ is the isentropic efficiency of the compressor under the design conditions, c_4 is the undetermined constant, which is generally set to be 0.3. Furthermore, $\dot{N}$ is the relative rotor speed of the compressor after correction, and $\dot{m}$ is the relative mass flow rate of the compressor after correction. They can be calculated by Equations (19) and (20), respectively.

$$\dot{N} = \frac{N}{N_d}\sqrt{\frac{T_{in,d}}{T_{in}}} \tag{19}$$

where N is the actual rotor speed, N_d is the design rotor speed, $T_{in,d}$ is the design inlet temperature of the compressor, and T_{in} is the actual inlet temperature of the compressor.

$$\dot{m} = \frac{m}{m_d}\frac{P_{in,d}}{P_{in}}\sqrt{\frac{T_{in}}{T_{in,d}}} \tag{20}$$

where $P_{in,d}$ is the designed inlet pressure of the compressor, and P_{in} is the actual inlet pressure of the compressor, m_d is the designed mass flow rate and m is the actual mass flow rate.

The relationship between the compression ratio of the compressor π_C and the relative mass flow rate $\dot{m}$ can be expressed as follows

$$\frac{\pi_C}{\pi_{C,d}} = c_1\dot{m}^2 + c_2\dot{m} + c_3 \tag{21}$$

where π_C is the actual compression ratio of the compressor, and $\pi_{C,d}$ is the compression ratio of the compressor under the design conditions. c_1, c_2 and c_3 are related correction coefficients obtained by fitting empirical equations, which can be calculated as follows

$$c_1 = \dot{N}/[p(1 - q/\dot{N}) + \dot{N}(\dot{N} - q)^2] \tag{22}$$

$$c_2 = (p - 2q\dot{N}^2)/[p(1 - q/\dot{N}) + \dot{N}(\dot{N} - q)^2] \tag{23}$$

$$c_3 = -(pq\dot{N} - q^2\dot{N}^3)/[p(1 - q/\dot{N}) + \dot{N}(\dot{N} - q)^2] \tag{24}$$

where p and q are experimental parameters, and p and q are set to be 0.36 and 1.06, respectively, for large axial flow devices.

For compressors, the isentropic efficiency and compression ratio under off-design conditions can be determined by the corrected mass flow rate and rotor speed. Based on the above equations, the compressor model can be established to study the effects of relative mass flow rate and relative rotor speed on compressor performances. With the change in relative mass flow rate and relative rotor speed, the change curves of relative isentropic efficiency and relative compression ratio of the compressor are shown in Figure 5. m/m_d is in the range of 0.3 to 1.1, N/N_d is in the range of 0.6 to 1.0, η_C varies from 0 to 100%, and π_C is greater than 1.

When N/N_d of the compressor is 1 and m/m_d increases from 0.88 to 1.04, $\eta_C/\eta_{C,d}$ of the compressor first increases from 0.98 to 1.00 and then decreases to 0.998, and $\pi_C/\pi_{C,d}$ decreases from 1.8 to 0.37. As N/N_d of the compressor increases from 0.6 to 1.0, the relative isentropic efficiency curves shown in Figure 5a tend to flatten out, and the peak value of $\eta_C/\eta_{C,d}$ and the corresponding m/m_d gradually increases. As shown in Figure 5b, as the ratio N/N_d increases, the relative compression ratio curves exhibit a tendency to steepen.

Simultaneously, there is a gradual decrease in $\pi_C/\pi_{C,d}$, with their peak values and the corresponding m/m_d gradually increasing.

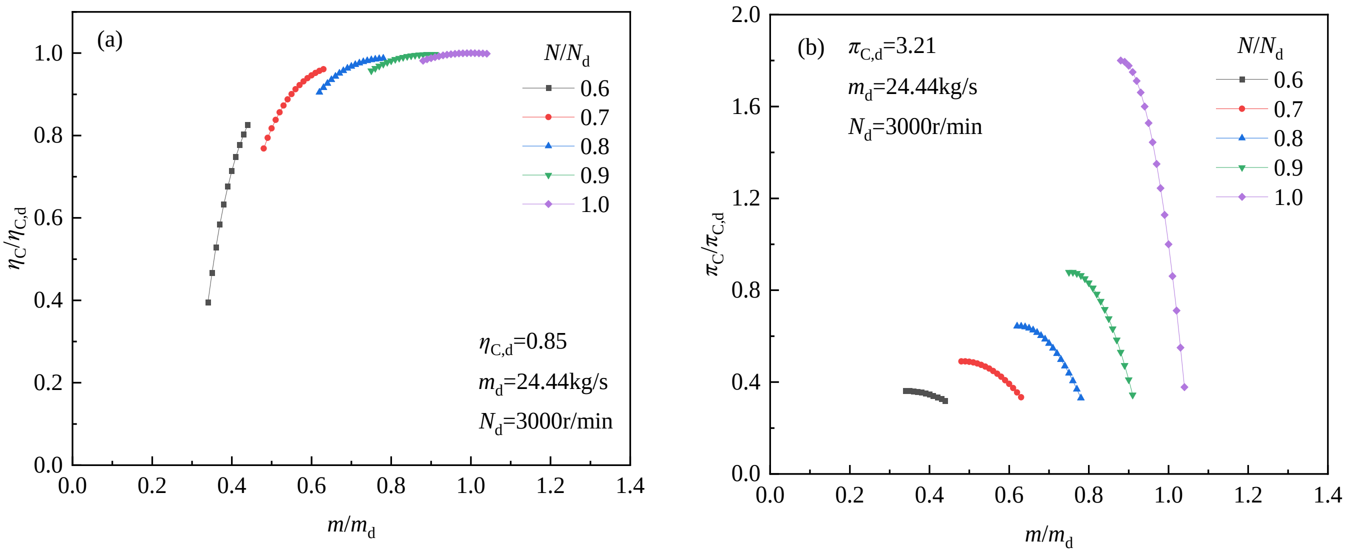

Figure 5. Effects of m/m_d on compressor performances. (**a**) Effect of m/m_d on relative isentropic efficiency; (**b**) effect of m/m_d on relative compression ratio.

As shown in Figure 6, the relative inlet temperature and relative rotor speed have significant effects on compressor performances. The range of $T_{in}/T_{in,d}$ is from 0.4 to 1.1, N/N_d is from 0.6 to 1.0, and η_C is from 0 to 100%. Furthermore, $\pi_C/\pi_{C,d}$ is in the range of 0–2 and π_C is greater than 1. As can be seen from the figure where N/N_d is constant, with the increase in $T_{in}/T_{in,d}$, the $\eta_C/\eta_{C,d}$ of the compressor increases rapidly at first, and then tends to be flat, while $\pi_C/\pi_{C,d}$ decreases significantly. When the N/N_d of the compressor increases from 0.6 to 1.0, the relative isentropic efficiency curves tend to be flat. However, the decline trend of the relative compression ratio curves become steep with the increase in N/N_d.

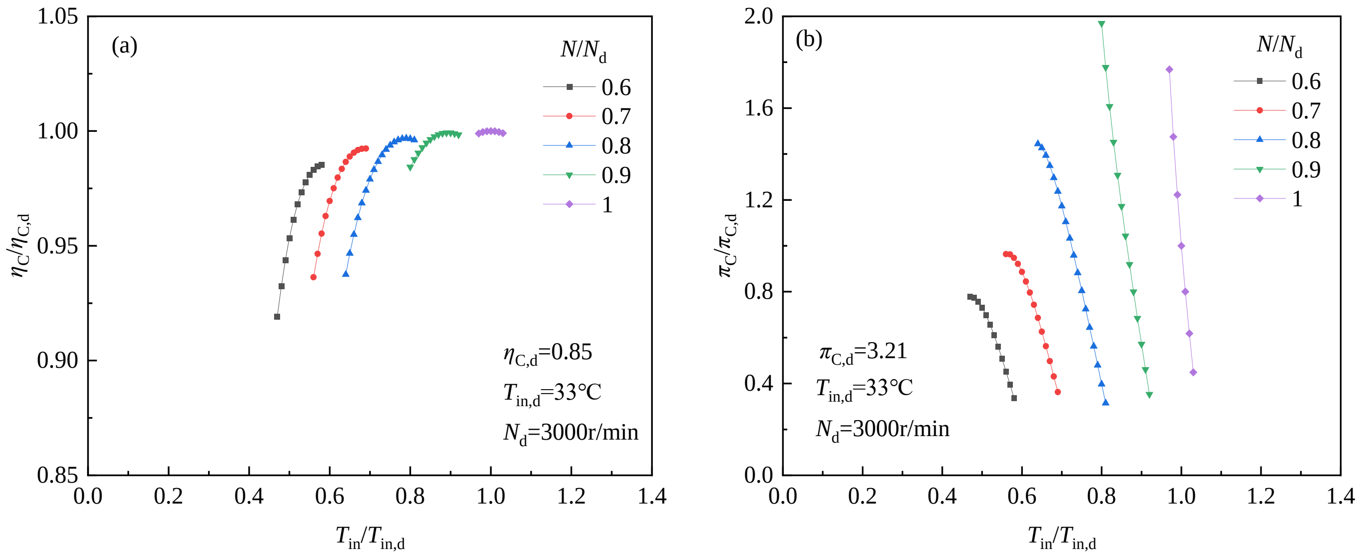

Figure 6. Effects of $T_{in}/T_{in,d}$ on compressor performances. (**a**) Effect of $T_{in}/T_{in,d}$ on relative isentropic efficiency; (**b**) effect of $T_{in}/T_{in,d}$ on relative compression ratio.

4.2. Modeling of Turbine

The isentropic efficiency η_T of the turbine under off-design conditions can be expressed by

$$\frac{\eta_T}{\eta_{T,d}} = \left[1 - 0.3\left(1 - \dot{N}\right)^2\right]\left(\frac{\dot{N}}{\dot{m}}\right)(2 - \frac{\dot{N}}{\dot{m}}) \tag{25}$$

where $\eta_{T,d}$ is the isentropic efficiency of the turbine under the design conditions, $\dot{N}$ is the relative rotor speed of the turbine after correction, $\dot{m}$ is the relative mass flow rate of the turbine after correction, and their calculation methods are the same as those of the compressor.

Furthermore, the mass flow rate m, rotor speed N, inlet temperature T_{in} and expansion ratio π_T of the turbine are mutually constrained, and the corresponding coupling relationship can be expressed as follows:

$$\frac{m}{m_d} = \sqrt{1.4 - 0.4\frac{N}{N_d}}\sqrt{\frac{T_{in}}{T_{in,d}}}\sqrt{\frac{(\pi_T{}^2 - 1)}{(\pi_{T,d}{}^2 - 1)}} \tag{26}$$

where π_T is the actual expansion ratio of the turbine, and $\pi_{T,d}$ is the expansion ratio of the turbine under the design conditions.

Based on the above control equations, the effects of relative mass flow rate and relative rotor speed on turbine performances are studied. The effects of m/m_d on the turbine relating to relative isentropic efficiency and the relative expansion ratio of the turbine are shown in Figure 7. The range of m/m_d is from 0.0 to 2.0, N/N_d is from 0.5 to 1.5, η_T is from 0 to 100%, and π_T is greater than 1. It can be seen that when N/N_d is 1 and m/m_d increases from 0.51 to 2.0, $\eta_T/\eta_{T,d}$ increases rapidly from 0.077 to 1, and then slowly decreases to 0.75, while $\pi_T/\pi_{T,d}$ increases from 0.576 to 1.926. When the N/N_d of the turbine increases from 0.5 to 1.5, the peak value of $\eta_T/\eta_{T,d}$ gradually increases from 0.925 to the maximum value 1 initially and then decreases to 0.925, while its corresponding m/m_d gradually increases, and the relative expansion ratio curves become steep. Furthermore, when the m/m_d of the turbine is 1 and N/N_d increases from 0.5 to 1.5, $\eta_T/\eta_{T,d}$ is symmetric with respect to N/N_d = 1, increasing from 0.694 to 1.00 and then decreasing to 0.694, while $\pi_T/\pi_{T,d}$ increases from 0.922 to 1.107.

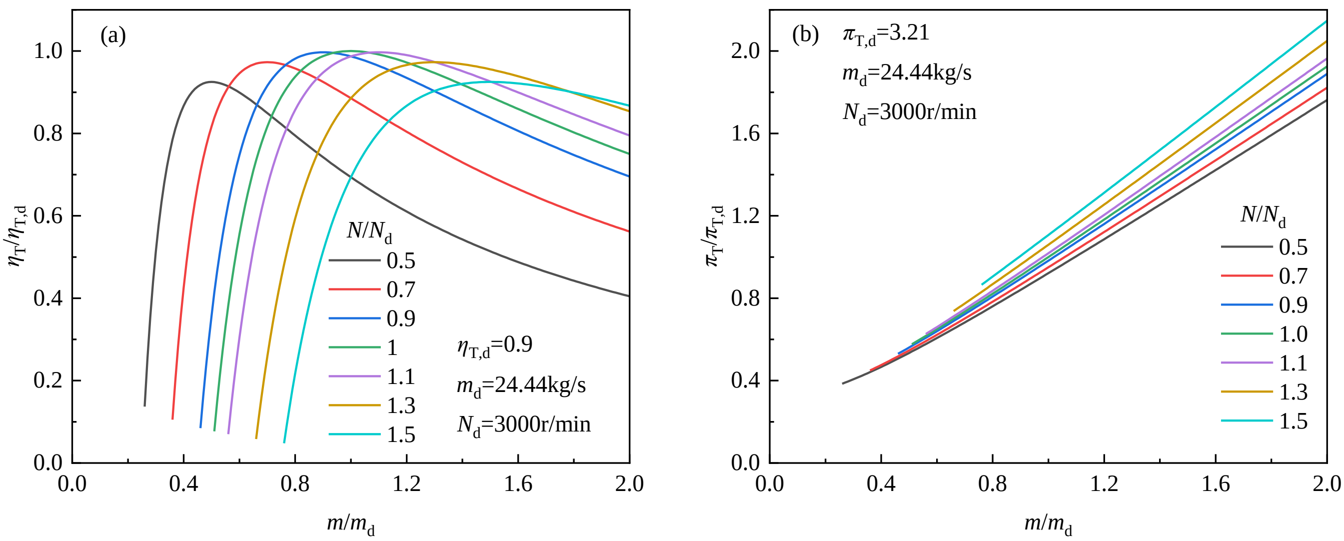

Figure 7. Effects of m/m_d on turbine performances. (**a**) Effect of m/m_d on relative isentropic efficiency; (**b**) effect of m/m_d on relative expansion ratio.

As shown in Figure 8, relative inlet temperature and relative rotor speed have significant effects on the isentropic efficiency and expansion ratio of the turbine. The range of $T_{in}/T_{in,d}$ is from 0.0 to 2.0, and the ranges of N/N_d, η_T and π_T are the same as those in Figure 7. When the N/N_d of the turbine is constant, with the increase in $T_{in}/T_{in,d}$, $\eta_T/\eta_{T,d}$ increases rapidly and then decreases slowly, while $\pi_T/\pi_{T,d}$ increases steadily. When N/N_d increases from 0.5 to 1.5, the peak value of $\eta_T/\eta_{T,d}$ remains basically unchanged, which increases from 0.975 to 1 and then decreases to 0.986, while the relative expansion ratio curves increase slowly.

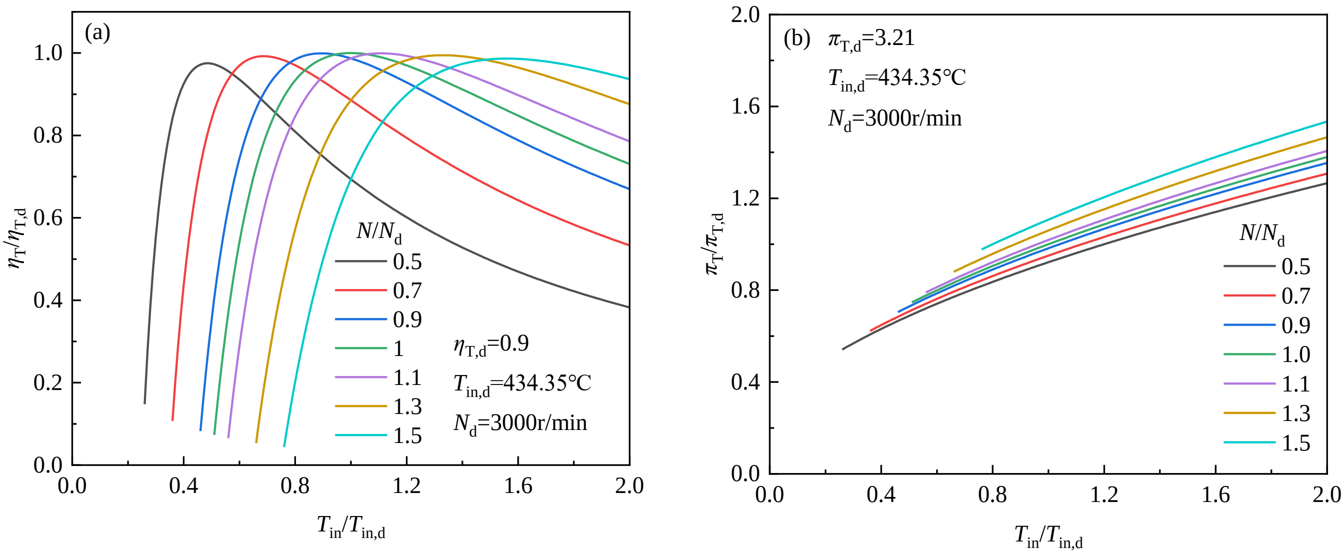

Figure 8. Effects of $T_{in}/T_{in,d}$ on turbine performances. (**a**) Effect of $T_{in}/T_{in,d}$ on relative efficiency; (**b**) effect of $T_{in}/T_{in,d}$ on relative expansion ratio.

5. Off-Design Performance Calculation of S-CO_2 Cycle

Based on the above solution methods of the system components, the off-design working condition models of the compressor, turbine and heat exchangers are programmed on the Matlab platform. In addition, the physical properties of CO_2, flue gas and water can be calculated by the REFPROP 9.0 software, based on known parameters. The corresponding calculation flow of the S-CO_2 power cycle under off-design working conditions is established, as shown in Figure 9. Firstly, the parameters, such as cold and heat source conditions, compressor inlet temperature and pressure, the mass flow rates of the working fluids and split ratio, are input. Then the models of the cooler, compressors, recuperators, turbines and heaters are calculated successively. Finally, the parameters of each state point are output, and the cycle performance parameters such as the net output work and cycle efficiency can be obtained.

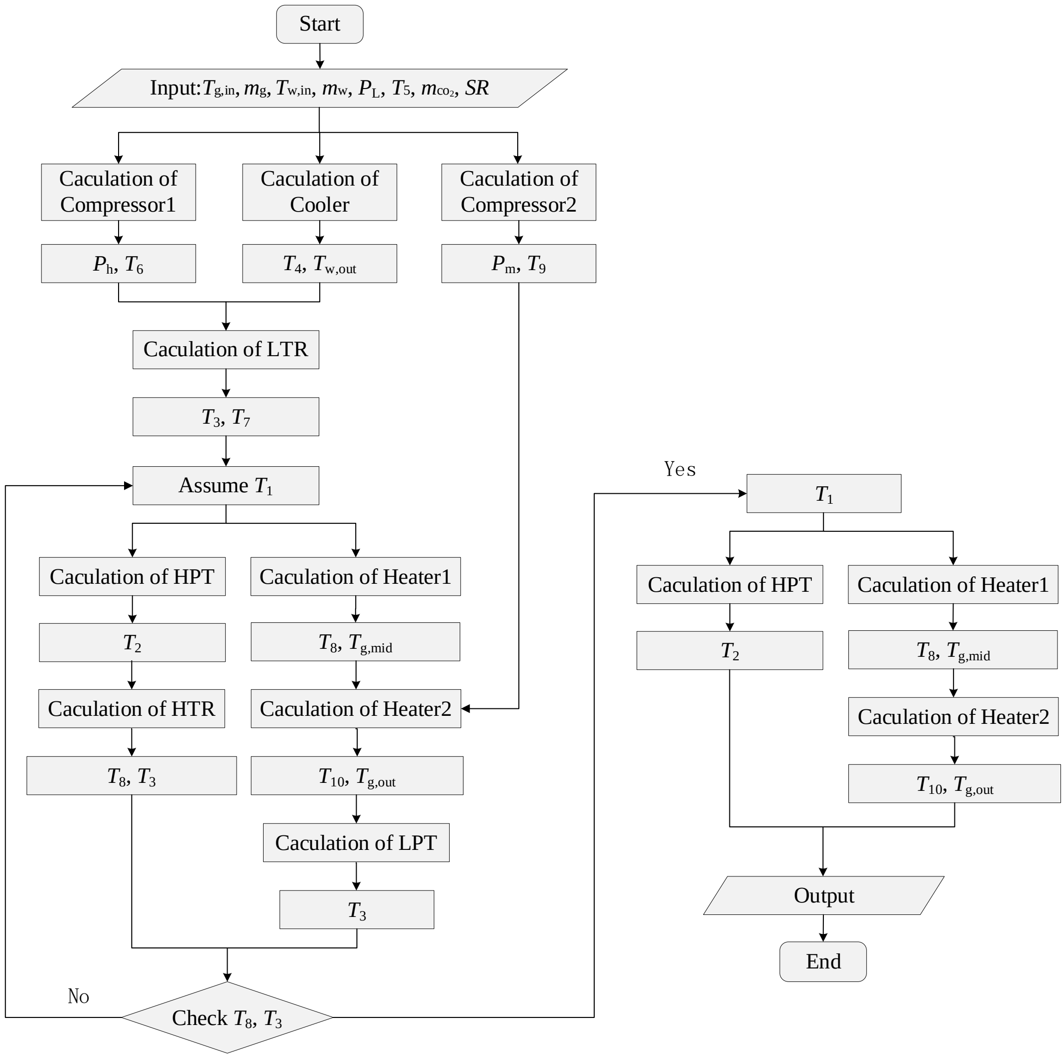

Figure 9. Calculation flow chart of the S-CO_2 cycle under off-design conditions.

6. Effects of Key System Parameters

During industrial production, cold and heat source parameters often fluctuate, which can impact the output parameters of system components and the performance of the cycle. In order to evaluate the system performances under off-design conditions, we analyze the cycle performances by controlling key variables such as cooling water inlet temperature, cooling water mass flow rate, flue gas inlet temperature and flue gas mass flow rate.

6.1. Effects of Cold Source Parameters

For the S-CO_2 power cycle that recovers flue gas waste heat, the cooling method is generally water cooling. In the actual production, the temperature of the cooling water is easily affected by the ambient temperature. Therefore, it is of practical significance to study the effects of cooling water parameters on the off-design characteristics of the system [34].

Under off-design conditions, the effects of cooling water inlet temperature on the system performances are analyzed when the other parameters are constant. As shown in Figure 10, the inlet temperature of the cooling water under the design working conditions is 25 °C, and the variation range of the inlet temperature is set at 23–27 °C. As the inlet temperature of the cooling water increases, the outlet temperature of the cooling water increases, and the inlet temperature T_4 and outlet temperature T_5 of the CO_2 side of the cooler gradually increase. As can be seen from Figure 6, the variation in the compressor inlet temperature has a weak effect on the isentropic efficiency, while it has a drastic effect on the compression ratio. Thus, the compression ratio gradually decreases as the compressor inlet temperature increases. With the increase in T_5 and the decrease in compressor outlet pressure, the compressor outlet temperature T_6 and T_9 increase correspondingly, and the compression work decreases first and then increases.

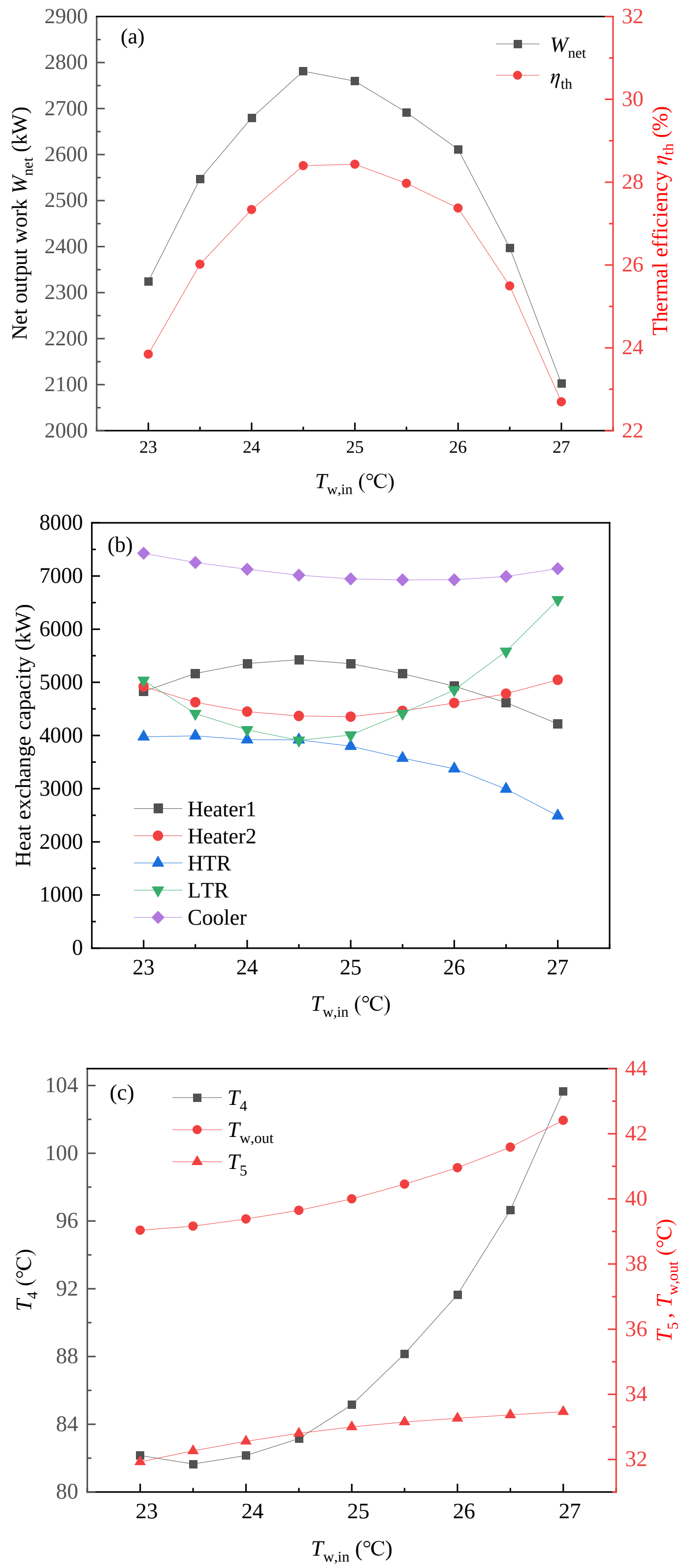

Figure 10. Effects of $T_{w,in}$ on system performances under off-design conditions. (**a**) W_{net}, η_{th}; (**b**) heat exchange capacity; (**c**) T_4, T_5, $T_{w,out}$.

As the CO_2 inlet temperature T_9 of Heater2 gradually increases, there is an initial decrease followed by an increase in outlet temperature T_{10}. The heat absorption in Heater2 also follows a similar trend, with the heat absorption first decreasing and then increasing as the inlet temperature slowly changes. When the CO_2 inlet temperature T_8 of Heater1 decreases first and then increases, the flue gas outlet temperature and CO_2 outlet temperature T_1 decreases first and then increases, while the flue gas inlet temperature remains constant. Consequently, the heat absorption in Heater1 initially increases but subsequently decreases.

From Figure 8a, it can be seen that the isentropic efficiency decreases as the turbine inlet temperature deviates from the design value at constant rotor speed. As shown in Figure 8b, due to the gradual decrease in the inlet pressure of the turbine, the rotor speed of the turbine is gradually reduced in order to maintain a stable low outlet pressure, resulting in a corresponding decrease in isentropic efficiency. Due to the effects of inlet temperature and rotor speed, both the outlet temperatures T_2 and T_3 of the turbines initially decrease and then increase, while total expansion work first increases and then decreases. Consequently, the net output work of the system increases from 2324.41 kW to 2781.11 kW and then decreases to 2102.63 kW. The total heat absorbed from the flue gas heat source follows the trend of initially increasing and subsequently decreasing, leading to an improvement in thermal efficiency from 23.85% to 28.43%, followed by a decline to 22.69%.

The impacts of the cooling water mass flow rate on the system's performance characteristics under off-design conditions are illustrated in Figure 11. The cooling water mass flow rate varies within the range of 0.8–1.2 times the design value. Within this investigated range, the CO_2 inlet and outlet temperatures T_4 and T_5 of the cooler gradually decrease as the cooling water mass flow rate increases. Simultaneously, there is a gradual decrease in compressor outlet temperatures T_6 and T_9, an increase in compressor outlet pressure, and a non-linear trend observed for total compression work with an initial decrease followed by an increase. Furthermore, the CO_2 outlet temperature T_{10} of the Heater2 exhibits a similar trend of first decreasing and then increasing. Compared to T_9, the variation in T_{10} is much greater, resulting in a fluctuating heat absorption for Heater2, characterized by an initial decrease followed by an increase. For Heater1, the flue gas outlet temperature $T_{g,mid}$ initially decreases and then increases while maintaining a constant flue gas inlet temperature. Therefore, the heat absorption first increases and then decreases.

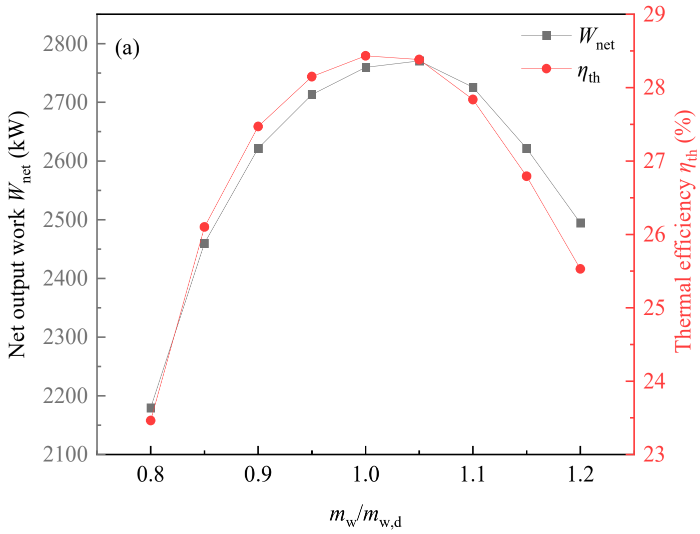

Figure 11. *Cont.*

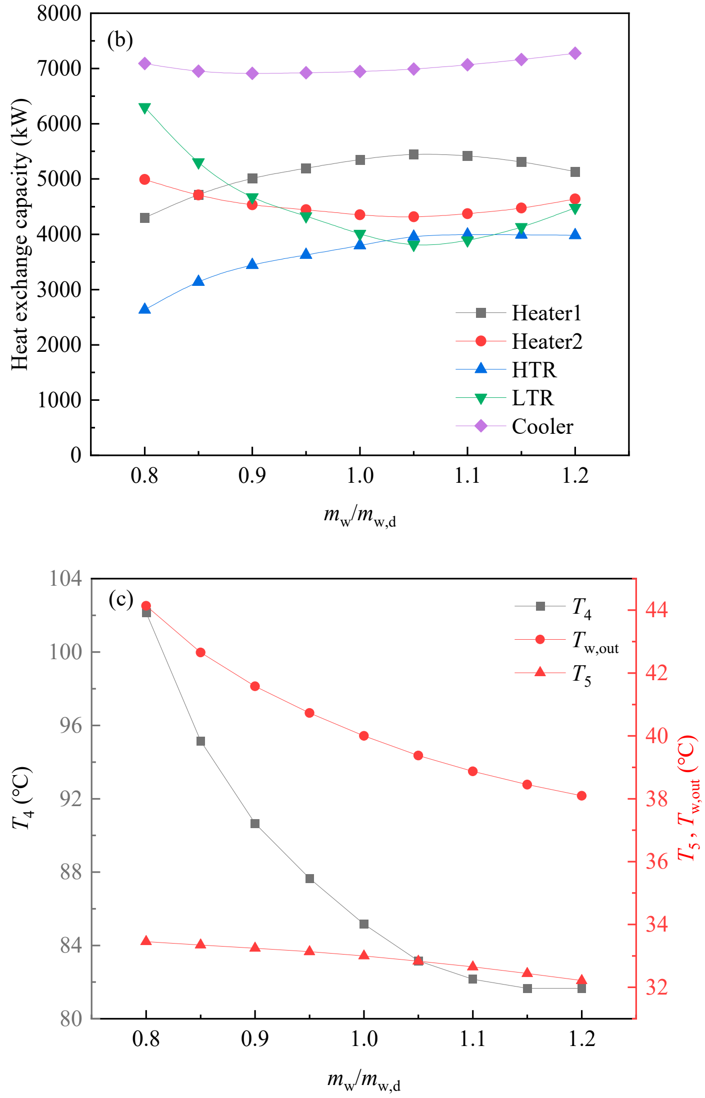

Figure 11. Effects of $m_w/m_{w,d}$ on system performances under off-design conditions. (**a**) W_{net}, η_{th}; (**b**) heat exchange capacity; (**c**) T_4, T_5, $T_{w,out}$.

As the medium and high pressures at the turbine inlet gradually increase, the turbine rotor speed gradually increases in order to keep the low pressure constant. Meanwhile, the isentropic efficiency and the total expansion work first increase and then decrease. Thus, the net output work of the system rises from 2179.45 kW to 2770.51 kW and then declines to 2494.5 kW. The total heat absorbed from the flue gas heat source experiences a slow increase followed by a decrease. As a result, the thermal efficiency increases from 23.46% to 28.43% and then decreases to 25.53%.

6.2. Effects of Heat Source Parameters

The impacts of the flue gas inlet temperature on the system performances under off-design conditions can be observed in Figure 12. With the flue gas inlet temperature $T_{g,in}$ increasing, both the flue gas outlet temperature $T_{g,mid}$ of Heater1 and $T_{g,out}$ of Heater2 gradually rise. As $T_{g,mid}$ increases faster than $T_{g,in}$ and $T_{g,out}$, the heat absorption in Heater1 gradually decreases while the heat absorption in Heater2 gradually increases.

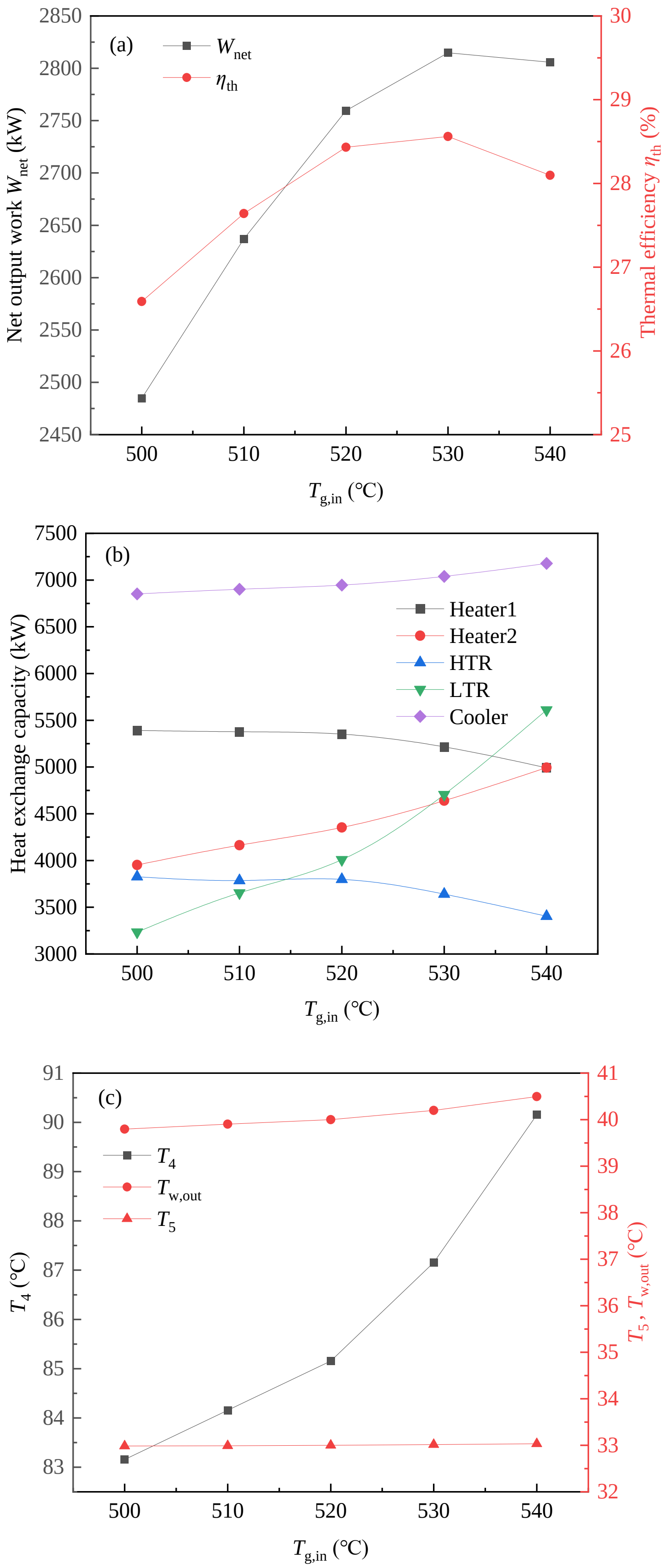

Figure 12. Effects of $T_{g,in}$ on system performances under off-design conditions. (**a**) W_{net}, η_{th}; (**b**) heat exchange capacity; (**c**) T_4, T_5, $T_{w,out}$.

The HPT inlet temperature T_1 rises with the flue gas inlet temperature, resulting in a corresponding gradual increase in expansion work. Similarly, the LPT inlet temperature T_{10} increases with the flue gas outlet temperature of Heater1, leading to an increase in the turbine outlet temperature T_3, and consequently the expansion work initially increases before decreasing.

Due to the small variations in compressor inlet and outlet temperatures, the compression work is less affected by the flue gas inlet temperature. Therefore, the net output work of the system increases from 2484.67 kW to 2814.88 kW, and then decreases to 2805.83 kW. The total heat absorbed from the flue gas heat source gradually increases, resulting in a rise in thermal efficiency from 26.59% to 28.56%, followed by a decrease to 28.1%.

The effects of the flue gas mass flow rate on the system performances under off-design conditions are depicted in Figure 13, with other input parameters held constant. The flue gas mass flow rate varies within the range of 0.85–1.15 times the design value. As the flue gas mass flow rate increases, the flue gas outlet temperatures of Heater1 and Heater2 gradually increase. However, as the flue gas inlet temperature remains constant, the overall heat absorption of Heater1 shows a decreasing trend. Furthermore, considering that the flue gas inlet temperature of Heater2 increases more rapidly than the outlet temperature, the heat absorption of Heater2 gradually increases.

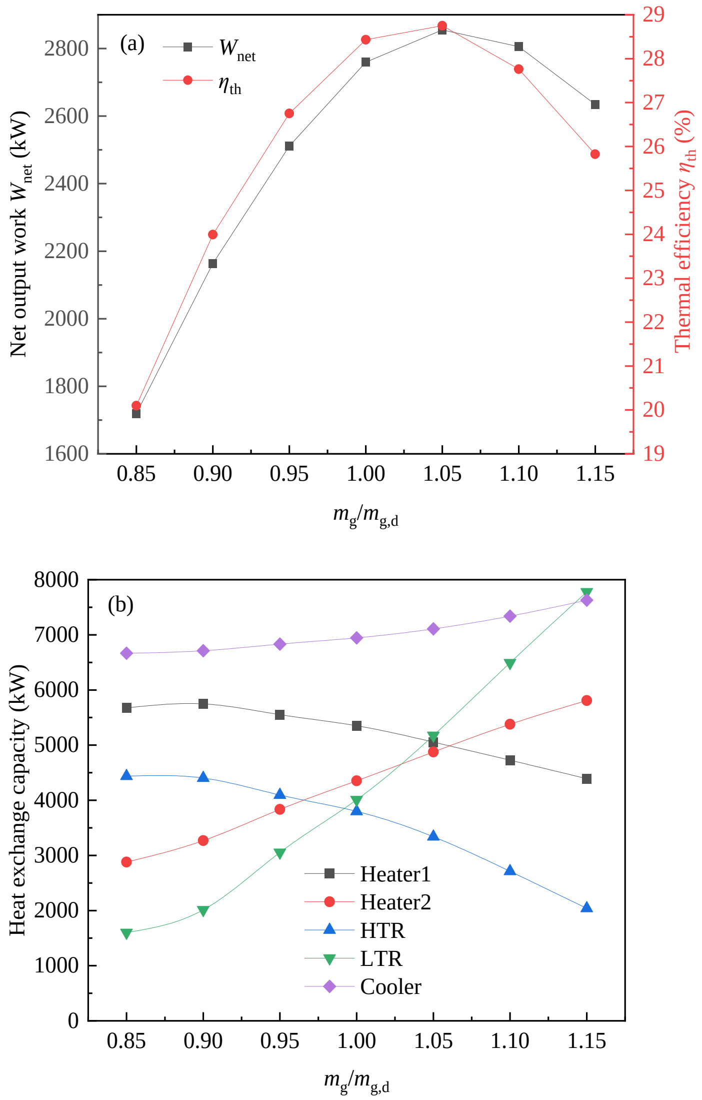

Figure 13. *Cont*.

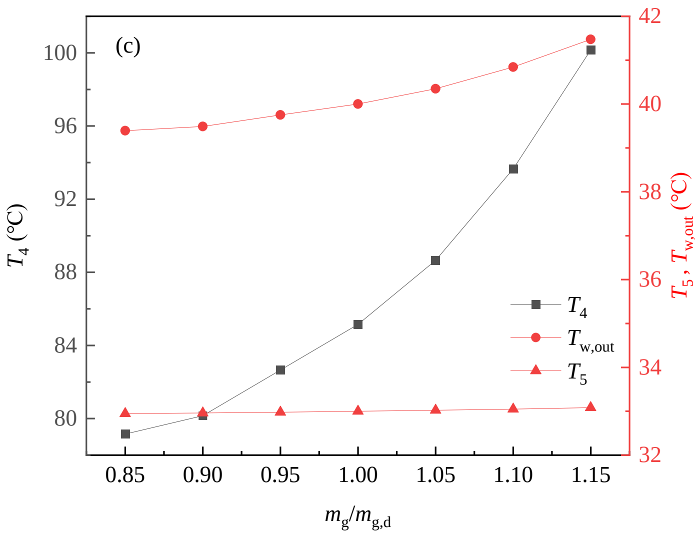

Figure 13. Effects of $m_g/m_{g,d}$ on system performances under off-design conditions. (**a**) W_{net}, η_{th}; (**b**) heat exchange capacity; (**c**) T_4, T_5, $T_{w,out}$.

The inlet temperature T_1 of the HPT rises with the increase in flue gas mass flow rate, leading to an increase and then a decrease in expansion work. Similarly, the inlet temperature T_{10} of the LPT increases with the increase in the flue gas outlet temperature of Heater1, resulting in an initial increase followed by a decrease in expansion work.

Given the slight changes in the compressor inlet and outlet temperatures, the compression work is less affected by the flue gas mass flow rate. Therefore, the net output work of the system increases from 1719.01 kW to 2855.09 kW and then decreases to 2634.58 kW. Furthermore, the total heat absorbed gradually increases, leading to an increase in thermal efficiency from 20.1% to 28.75%, followed by a decrease to 25.83%.

7. Control Strategy of the Cooling Process

Based on the above analysis, it can be seen that the inlet temperature and mass flow rate of cooling water have great effects on the system performance. When the inlet temperature of the cooling water increases from 23 °C to 27 °C, compared with the optimal value, the net output work of the cycle decreases by up to 24.4% and the cycle thermal efficiency decreases by up to 20.19%. In actual production, the cooling water inlet temperature is easily affected by natural environmental conditions, and the compressor performance is significantly affected by the cooling water inlet temperature, thus affecting the overall performances of the system. Therefore, when the inlet temperature of the cooling water fluctuates, in order to ensure the efficient and stable operation of the system, it is necessary to develop the corresponding control strategy.

Compared with regulating the flue gas inlet temperature and flue gas mass flow rate, it is more convenient to adjust the cooling water mass flow rate to reduce the effect of the cooling water inlet temperature on the system. Meanwhile, it has less effect on other parameters of the system, and it is easy to operate in actual production. Therefore, the effect of the cooling water inlet temperature is controlled by regulating the cooling water mass flow rate.

By changing the cooling water mass flow rate, the temperature changes on the CO_2 side of the cooler can be attenuated. In this paper, the CO_2 outlet temperature T_5 of the cooler is set to the design value, and the range of the cooling water mass flow rate is set based on the design value. The optimal value can be found by the exhaustive method to make T_4 closer to the design value. Based on the cooling water mass flow rate control strategy, the parameter changes in the cooler are shown in Figure 14. In order to make the parameters on the CO_2 side closer to the design values, when the inlet temperature of cooling water increases from 23 °C to 27 °C, the mass flow rate of the cooling water will increase from 82.3% to 132.7% of the design value, and the outlet temperature of the cooling water will decrease from 41.23 °C to 38.3 °C.

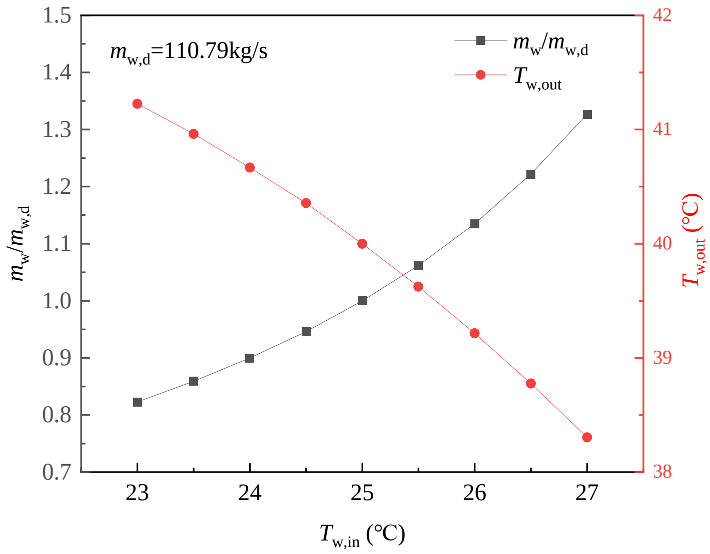

Figure 14. Variation in the cooler parameters.

8. Conclusions

In this paper, the thermal performance and control strategy of an innovative S-CO_2 power cycle driven by flue gas waste heat are investigated under off-design conditions. According to the design parameters of the S-CO_2 cycle, the off-design models of system components including the turbine, compressor, printed circuit heat exchangers and shell-and-tube heat exchangers are first established. Then, under off-design conditions, performance characteristics of the system are analyzed and discussed. Finally, aiming at the S-CO_2 cooling process, the control strategy of the cooling water flow is proposed to match the inlet temperature variation in cooling water. The main conclusions can be drawn as follows:

(1) When the inlet temperature and mass flow rate of the cooling water change, the cycle efficiency can reach the maximum value of 28.43% at the design point. When the flue gas inlet temperature changes, the maximum cycle efficiency 28.56% is obtained at 530 °C. For the variation of the flue gas mass flow rate, at the mass flow ratio 1.05, the cycle efficiency reaches the peak of 28.75%.

(2) To ensure the efficient and stable operation of the S-CO_2 power cycle, a control strategy of the cold end is proposed for the inlet temperature variation in the cooling water. When the cooling water inlet temperature increases from 23 °C to 27 °C, the cooling water mass flow rate should increase from 82.3% to 132.7% of the design value.

Based on the research in this paper, more control strategies will be studied in the future so as to deal with different changes in working conditions, such as flue gas parameter variations and rotational speed variations. In addition, the dynamic characteristics of the S-CO_2 cycle will be further investigated to reveal the parameter variations in the system under full operating conditions. On this basis, relevant control methods will be proposed to guide the operation of a practical engineering system.

Author Contributions: Conceptualization, R.D.; Methodology, Y.L.; Software, W.S.; Validation, L.X.; Writing—original draft, S.H.; Writing—review & editing, X.L.; Supervision, N.Z. All authors have read and agreed to the published version of the manuscript.

Funding: This work is sponsored by the National Natural Science Foundation of China (52106037). Furthermore, the work is also supported by Central South University Innovation-Driven Research Program (2023CXQD056), and Graduate Research Innovation Project of Central South University.

Data Availability Statement: The original contributions presented in the study are included in the article, further inquiries can be directed to the corresponding author.

Conflicts of Interest: Authors Ruochen Ding and Xinxing Lin were employed by the company China Three Gorges Corporation Science and Technology Research Institute. The remaining authors declare that the research was conducted in the absence of any commercial or financial relationships that could be construed as a potential conflict of interest.

Nomenclature

Symbols

S-CO_2	Supercritical carbon dioxide
PCHE	Printed circuit heat exchanger
ORC	Organic rankine cycle
SRC	Simple recuperative cycle
PC	Precompression cycle
RC	Recompression cycle
PCC	Partial cooling cycle
ICC	Intermediate cooling cycle
T-CO_2	Transcritical carbon dioxide
LTR	Low-temperature recuperator
HTR	High-temperature recuperator
HPT	High-pressure turbine
LPT	Low-pressure turbine
PPTD	Pinch point temperature difference (°C)
W_{net}	Net output work (kW)
T	Temperature (°C)
P	Pressure (MPa)
s	Specific entropy (kJ/(kg·K))
m	Mass flow rate (kg/s)
h	Specific enthalpy (kJ/kg) or convective heat transfer coefficients (kW/(m^2·K))
Q	Heat transfer rate (kW)
a	Number of channels
n	Number of single channel unit elements
A	Heat exchange area (m^2)
k	Local heat transfer coefficient (kW/(m^2·K))
R_{w}	Conductive thermal resistance of the channel wall ((m^2·K)/kW)
d_{hy}	Hydraulic diameter (mm)
Nu	Nusselt number
Re	Reynold number
Pr	Prandtl number
u_{o}	The flow velocity passing through the maximum cross-sectional area between pipes (m/s)
w_{ch}	Channel width (mm)
d_{ch}	Channel height (mm)
t_{p}	Plate thickness (mm)
w_{f}	Fin width (mm)
A_{flow}	Flow area of the channel (m^2)
K	Total heat transfer coefficient (kW/(m^2·K))
A_{i}	Inside heat transfer area of heat transfer tube (m^2)
A_{o}	Outside heat transfer area of heat transfer tube (m^2)
A_{m}	Average heat transfer area of heat transfer tube (m^2)
d	Diameter (m)
d_{e}	Feature size (m)
P_{t}	Center distance of the tubes (m)
A_{s}	Maximum cross-sectional area between tubes (m^2)
l_{b}	Baffle spacing (m)
D_{i}	Inner diameter of the shell (m)
n_{c}	Number of tubes across the centerline of the bundle

N_t	Number of the tubes
A_f	Shell side flow area (m^2)
N	Rotor speed (r/min)
SR	Split ratio
Greek symbols	
η_{th}	Thermal efficiency (%)
λ	Thermal conductivity of the fluid (kW/(m·K))
λ_w	Thermal conductivity of the channel wall or tube wall, (kW/(m·K))
α_i	Heat transfer coefficient inside the tube (kW/(m^2·K))
α_o	Heat transfer coefficient outside the tube (kW/(m^2·K))
δ	Thickness of the tube wall (m)
ρ	Density (kg/m^3)
μ	Dynamic viscosity (kg/(m·s))
π_C	Compression ratio
π_T	Expansion ratio
Subscripts	
c	Critical or cold fluid
ch	Channel
h	Hot fuid or high pressure
i	Inside
o	Outside
in	Inlet
w	Wall or water
out	Outlet
L	Low pressure
m	Medium pressure
g	Flue gas
mid	Flue gas outlet of Heater1
C	Compressor
d	Design condition
T	Turbine

References

1. Chen, S.; Zheng, Y.; Wu, M.; Hu, J.; Xiang, W. Thermodynamic analysis of oxy-fuel combustion integrated with the sCO_2 Brayton cycle for combined heat and power production. *Energy Convers. Manag.* **2021**, *232*, 113869. [CrossRef]
2. Kareem, P.H.; Ali, M.; Tursoy, T.; Khalifa, W. Testing the Effect of Oil Prices, Ecological Footprint, Banking Sector Development and Economic Growth on Energy Consumptions: Evidence from Bootstrap ARDL Approach. *Energies* **2023**, *16*, 3365. [CrossRef]
3. Wang, X.; Zhang, M. The Thermal Economy of a Circulating Medium and Low Temperature Waste Heat Recovery System of Industrial Flue Gas. *Int. J. Heat Technol.* **2021**, *39*, 1680–1688. [CrossRef]
4. Gao, B.; Sun, Z. Marginal CO_2 and SO_2 Abatement Costs and Determinants of Coal-Fired Power Plants in China: Considering a Two-Stage Production System with Different Emission Reduction Approaches. *Energies* **2023**, *16*, 3488. [CrossRef]
5. Larjola, J. Electricity from industrial waste heat using high-speed organic Rankine cycle (ORC). *Int. J. Prod. Econ.* **1995**, *41*, 227–235. [CrossRef]
6. Wang, E.; Peng, N. A Review on the Preliminary Design of Axial and Radial Turbines for Small-Scale Organic Rankine Cycle. *Energies* **2023**, *16*, 3423. [CrossRef]
7. Loni, R.; Najafi, G.; Bellos, E.; Rajaee, F.; Mazlan, M. A review of industrial waste heat recovery system for power generation with Organic Rankine Cycle: Recent Challenges and Future Outlook. *J. Clean. Prod.* **2020**, *287*, 125070. [CrossRef]
8. Carrillo Caballero, G.; Cardenas Escorcia, Y.; Venturini, O.J.; Silva Lora, E.E.; Alviz Meza, A.; Mendoza Castellanos, L.S. Unidimensional and 3D Analyses of a Radial Inflow Turbine for an Organic Rankine Cycle under Design and Off-Design Conditions. *Energies* **2023**, *16*, 3383. [CrossRef]
9. Zhang, R.; Su, W.; Lin, X.; Zhou, N.; Zhao, L. Thermodynamic analysis and parametric optimization of a novel S–CO_2 power cycle for the waste heat recovery of internal combustion engines. *Energy* **2020**, *209*, 118484. [CrossRef]
10. Guo, J.; Li, M.; He, Y.; Jiang, T.; Ma, T.; Xu, J.; Cao, F. A systematic review of supercritical carbon dioxide(S-CO_2) power cycle for energy industries: Technologies, key issues, and potential prospects. *Energy Convers. Manag.* **2022**, *258*, 115437. [CrossRef]
11. Yu, A.; Xing, L.; Su, W.; Liu, P. State-of-the-art review on the CO_2 combined power and cooling system: System configuration, modeling and performance. *Renew. Sustain. Energy Rev.* **2023**, *188*, 113775. [CrossRef]
12. White, M.T.; Bianchi, G.; Chai, L.; Tassou, S.A.; Sayma, A.I. Review of supercritical CO_2 technologies and systems for power generation. *Appl. Therm. Eng.* **2021**, *185*, 116447. [CrossRef]

13. Liang, Y.; Lin, X.; Su, W.; Xing, L.; Zhou, N. Thermal-economic analysis of a novel solar power tower system with CO_2-based mixtures at typical days of four seasons. *Energy* **2023**, *276*, 127602. [CrossRef]
14. Rahbari, H.R.; Mandø, M.; Arabkoohsar, A. A review study of various High-Temperature thermodynamic cycles for multigeneration applications. *Sustain. Energy Technol. Assess.* **2023**, *57*, 103286. [CrossRef]
15. Liao, J.; Liu, X.; Zheng, Q.; Zhang, H. Analysis of supercritical CO_2 power generation cycle characteristics. *Therm. Power Eng.* **2016**, *31*, 40−46+149−150. [CrossRef]
16. Fang, Z.; Dong, X.; Tang, X. Research on gas engine waste heat recovery system based on S-CO_2. *Combust. Sci. Technol.* **2023**, *29*, 543–551.
17. Fu, J. Research on Optimization of Supercritical Carbon Dioxide Brayton Cycle Thermodynamic System. Master's Thesis, North China Electric Power University, Beijing, China, 2020.
18. Lock, A.; Bone, V. Off-design operation of the dry-cooled supercritical CO_2 power cycle. *Energy Convers. Manag.* **2022**, *251*, 114903. [CrossRef]
19. Duniam, S.; Veeraragavan, A. Off-design performance of the supercritical carbon dioxide recompression Brayton cycle with NDDCT cooling for concentrating solar power. *Energy* **2019**, *187*, 115992. [CrossRef]
20. Xiao, G.; Yu, A.; Lin, X.; Su, W.; Zhou, N. Constructing a novel supercritical carbon dioxide power cycle with the capacity of process switching for the waste heat recovery. *Int. J. Energy Res.* **2022**, *46*, 5099–5118. [CrossRef]
21. Wu, C.; Wang, S.-S.; Bai, K.-L.; Li, J. Thermodynamic analysis and parametric optimization of CDTPC-ARC based on cascade use of waste heat of heavy-duty internal combustion engines (ICEs). *Appl. Therm. Eng.* **2016**, *106*, 661–673. [CrossRef]
22. Huang, J.; Han, Z.; Guo, J.; Huai, X. Research progress of supercritical CO_2 microchannel heat exchangers. *J. Refrig.* **2023**, *44*, 1–14.
23. Rao, Z.; Xue, T.; Huang, K.; Liao, S. Multi-objective optimization of supercritical carbon dioxide recompression Brayton cycle considering printed circuit recuperator design. *Energy Convers. Manag.* **2019**, *201*, 112094. [CrossRef]
24. Wang, Z.; Zhu, Y.; Wang, F.; Wang, P.; Liu, J. In Proceedings of the 11th International Symposium on Heating, Ventilation and Air Conditioning (ISHVAC 2019): Volume III: Buildings and Energy; Springer: Berlin/Heidelberg, Germany, 2020.
25. Ngo, T.L.; Kato, Y.; Nikitin, K.; Tsuzuki, N. New printed circuit heat exchanger with S-shaped fins for hot water supplier. *Exp. Therm. Fluid Sci.* **2006**, *30*, 811–819. [CrossRef]
26. Gnielinski, V. New equations for heat and mass transfer in the turbulent flow in pipes and channels. In *NASA STI/Recon Technical Report A*; NASA/ADS: Washington, DC, USA, 1975; Volume 41.
27. Dittus, F.W.; Boelter, L.M.K. Heat transfer in automobile radiators of the tubular type. *Int. Commun. Heat Mass Transf.* **1985**, *12*, 3–22. [CrossRef]
28. Zhang, Z.; Liu, J.; Wang, S.; Zheng, W. Thermodynamic calculation and numerical simulation of shell-and-tube heat exchangers. *Non-Ferr. Metall. Energy Effic.* **2012**, *28*, 34−38+28.
29. Tun, C.M.; Fane, A.G.; Matheickal, J.T.; Sheikholeslami, R. Membrane distillation crystallization of concentrated salts-Flux and crystal formation. *J. Membr. Sci.* **2005**, *257*, 144–155. [CrossRef]
30. Qi, F. Advances in heat transfer calculation methods for shell-and-shell heat exchangers without phase change. *Pharm. Eng.* **2002**, *23*, 29–36.
31. Jeong, Y.; Son, S.; Cho, S.K.; Baik, S.; Lee, J.I. Evaluation of supercritical CO_2 compressor off-design performance prediction methods. *Energy* **2020**, *213*, 119071. [CrossRef]
32. Wang, W.; Cai, R.; Zhang, N. General characteristics of single shaft microturbine set at variable speed operation and its optimization. *Appl. Therm. Eng.* **2004**, *24*, 1851–1863. [CrossRef]
33. Zhang, N.; Cai, R. Analytical solutions and typical characteristics of part-load performance of single shaft gas turbine and its cogeneration. *Energy Convers. Manag.* **2002**, *43*, 1323–1337. [CrossRef]
34. Poškas, R.; Sirvydas, A.; Kulkovas, V.; Poškas, P.; Jouhara, H.; Miliauskas, G.; Puida, E. Flue Gas Condensation in a Model of the Heat Exchanger: The Effect of the Cooling Water Flow Rate and Its Temperature on Local Heat Transfer. *Appl. Sci.* **2022**, *12*, 12650. [CrossRef]